AGU PUBLICATIONS

JGR

Journal of Geophysical Research: Oceans

RESEARCH ARTICLE

10.1002/2016JC012276

Key Points:

- Phytoplankton respond to El Niño at different time lags, depending on the location
- Within the El Niño period, Chl *a* changes between basin-scale high and basin-scale low
- Wind speed, wind circulation, and river discharge are responsible for basin-scale Chl *a* dynamics

Correspondence to:
E. Siswanto,
ekosiswanto@jamstec.go.jp

Citation:
Siswanto, E., H. Ye, D. Yamazaki, and D.L. Tang (2017), Detailed spatiotemporal impacts of El Niño on phytoplankton biomass in the South China Sea, *J. Geophys. Res. Oceans*, *122*, doi:10.1002/2016JC012276.

Received 25 AUG 2016
Accepted 6 MAR 2017
Accepted article online 11 MAR 2017

Detailed spatiotemporal impacts of El Niño on phytoplankton biomass in the South China Sea

Eko Siswanto[1], Haijun Ye[2], Dai Yamazaki[3], and DanLing Tang[2]

[1]Department of Environmental and Geochemical Cycle Research, Japan Agency for Marine-Earth Science and Technology, Yokohama, Japan, [2]State Key Laboratory of Tropical Oceanography, South China Sea Institute of Oceanology, Chinese Academy of Sciences, Guangzhou, China, [3]Department of Integrated Climate Change Projection Research, Japan Agency for Marine-Earth Science and Technology, Yokohama, Japan

Abstract The lagging and leading correlations among satellite observations, reanalyzed biogeophysical data, and the Nino3.4 El Niño index were investigated to reveal the impacts of El Niño on the phytoplankton biomass (chlorophyll *a* [Chl *a*]) in the South China Sea (SCS), in an attempt to identify the probable responsible factors in greater spatiotemporal detail. A basin-scale high Chl *a* concentration during the developing phase of El Niño changed to basin-scale low Chl *a* during the weakening phase. Cyclonic wind circulation in the northern basin, increased wind speed in the southern basin, and strengthened upwelling off the Vietnamese coast likely caused a basin-scale nutrient increase during the developing phase of an El Niño event; the opposite conditions led to low nutrient levels during the weakening phase. Decreases in Chl *a* east of the Vietnamese coast and northwest of Borneo Island were due to decreases in nutrients supplied by rivers. These spatiotemporal changes are considered biogeophysical responses to a variety of types of El Niño. Regardless of the El Niño type, reanalyzing biogeophysical data sets during central Pacific warming separately from those during eastern Pacific warming is recommended for a more robust understanding of the detailed spatiotemporal impacts of different El Niño types on the biogeophysical environment of the SCS.

1. Introduction

The capacity of the oceans to support fisheries production through the marine food chain, and to remove atmospheric carbon dioxide biologically through the so-called “biological pump,” largely depends on the variability in phytoplankton biomass and primary productivity commonly indexed by surface chlorophyll *a* concentration (Chl *a*, mg m^{-3}) [e.g., *Deuser et al.*, 1990; *Huot et al.*, 2007; *Iverson*, 1990; *Friedland et al.*, 2012]. The previous studies cited in this paper describe either phytoplankton biomass or primary productivity variability. However, we use Chl *a* to collectively describe both phytoplankton biomass (carbon standing stock) and primary productivity (carbon fixation rate), because primary productivity is largely determined by phytoplankton biomass at both global and regional scales [e.g., *Behrenfeld and Falkowski*, 1997; *Tan and Shi*, 2009].

By modifying coupled atmosphere-ocean interactions, global climate changes drive variability in Chl *a* at both global and basin scales [e.g., *Behrenfeld et al.*, 2006; *Martinez et al.*, 2009; *Siswanto et al.*, 2016a,2016b]. Understanding the main mechanisms through which global climate change affects ocean Chl *a* is thus of particular interest in studies on the possible changes in ocean biogeochemical cycle processes and ocean productivity status under future climate change scenarios. This is particularly important in marginal seas, where the interplay of numerous mechanisms is more complex than that in the open oceans, and where human activities are concentrated.

Previous studies have shown that through atmospheric teleconnection, the climate anomaly of El Niño affects surface Chl *a* in the South China Sea (SCS), the largest marginal sea in the northwestern Pacific Ocean [*Zhao and Tang*, 2007; *Tan and Shi*, 2009; *Palacz et al.*, 2011; *Liao et al.*, 2012; *Sun*, 2017]. El Niño influences Chl *a* in the SCS by modifying physical oceanographic processes that change nutrient availability, because phytoplankton in the SCS are more limited by nutrient versus light availability [*Palacz et al.*, 2011; *Liao et al.*, 2012]. *Zhao and Tang* [2007] and *Tan and Shi* [2009] attributed a decline in Chl *a* in summer 1998 in the western SCS to weakening Ekman pumping and upwelling caused by weakening East Asian monsoon southwesterly winds associated with the 1997/1998 El Niño event.

In addition, *Palacz et al*. [2011] and *Liao et al*. [2012] reported changes in Chl *a* related to El Niño across the SCS basin. *Palacz et al*. [2011] reported an increase in Chl *a* over the SCS basin from 1997 to 2003, implicitly indicating low Chl *a* at the beginning of their time series (i.e., strong El Niño). Applying empirical orthogonal function (EOF) analysis, *Liao et al*. [2012] further showed that Chl *a* in the SCS responds differently to different types of El Niño. The authors reported that, whereas a basin-scale decrease in Chl *a* was associated with canonical El Niño with a 4 month lag (El Niño leading), an increase in Chl *a* in the central and eastern SCS was associated with the El Niño Modoki state [*Ashok et al*., 2007] with no time lag. *Liao et al*. [2012] further attributed a canonical El Niño-related basin-scale decrease in Chl *a* to Ekman downwelling, and El Niño Modoki-related Chl *a* increases in the central and eastern SCS to Ekman upwelling. *Sun* [2017] recently attributed a decline in Chl *a* along the northwestern coast of Borneo Island during El Niño to a reduction in the level of nutrients supplied by local rivers.

The above mentioned studies clearly indicate the existence of spatiotemporal variation in the Chl *a* response to El Niño events in the SCS. There are also indications that physical factors (e.g., Ekman upwelling/downwelling, atmospheric/ocean circulations, and warming/cooling surface) that drive Chl *a* variability also exhibit responses to El Niño according to various spatiotemporal patterns [e.g., *Wang et al*., 2006; *Lan et al*., 2012; *Liao et al*., 2012]. However, detailed spatiotemporal evolutions, such as shrinking/expanding areas of low/high Chl *a* [*Palacz et al*., 2011], decreases/increases in Chl *a* [*Liao et al*., 2012], and their relationships to geophysical changes with different time lags and areas of extension in response to El Niño events, have not been clearly identified.

Therefore, this study aimed to identify in detail the spatiotemporal Chl *a* evolution in the SCS related to El Niño, based on satellite ocean color observations. By examining features of the El Niño impacts on satellite-derived and/or reanalyzed geophysical data, we also identified the probable factors underlying the observed spatiotemporal effects of El Niño on Chl *a*.

2. Methodology

2.1. Satellite and Reanalyzed Data

The satellite data used in this study included monthly phytoplankton Chl *a* and photosynthetically available radiation (PAR, Einstein m^{-2} d^{-1}) retrieved by the Sea-viewing Wide Field-of-view Sensor (SeaWiFS) (http://oceancolor.gsfc.nasa.gov), monthly sea surface temperature (SST, °C) retrieved by the Advanced Very High Resolution Radiometer (AVHRR) (http://podaac.jpl.nasa.gov) and the Moderate Resolution Imaging Spectroradiometer (MODIS) (http://oceancolor.gsfc.nasa.gov), and monthly wind fields [i.e., wind speed (WS, m s^{-1}), zonal wind speed (UW, m s^{-1}), and meridional wind speed (VW, m s^{-1})], which are processed by the Cross-Calibrated Multi-Platform (CCMP) project (http://podaac.jpl.nasa.gov).

As proxies of terrigenous nutrient input to the coastal regions of the SCS, we also analyzed rain rate (RR, mm h^{-1}) and river discharge (m^3 s^{-1}) data. Data for RR were retrieved from the Tropical Rainfall Measuring Mission (TRMM) archive maintained by the Asia-Pacific Data Research Center (http://apdrc.soest.hawaii.edu). We estimated river discharge using the global river hydrodynamic model CaMa-Flood [*Yamazaki et al*., 2011, 2013], which simulates surface water dynamics (river discharge, floodplain inundation, water level, and water volume) using a shallow water flow equation. The river discharge simulation was executed using the HydroSHEDS river network [*Lehner and Grill*, 2013] at 0.25° spatial resolution, while floodplain inundation was treated as subgrid physics based on the SRTM3 DEM [*Farr et al*., 2007]. The CaMa-Flood model was forced by runoff calculated by the land surface model MATSIRO under JRA-25 reanalysis-based atmospheric boundary conditions [*Kim et al*., 2009]. Details of the CaMa-Flood simulation and validation have been explained in previous papers [*Yamazaki et al*., 2011, 2013]. We selected river discharge data from the Mekong River and Rajang-Kapit Wharf River mouths. The Mekong River is known to supply nutrients to waters east of the Vietnamese coast, driving Chl *a* variability [e.g., *Tang et al*., 2004]. We considered discharge from Rajang-Kapit Wharf River to be a proxy for the discharge from all rivers in northwestern Borneo that supply nutrients to the northwestern coast of Borneo Island [e.g. *Sun*, 2017].

We used monthly mixed layer depth (MLD, m) data that had been reanalyzed by the Global Ocean Reanalysis System (GLORS, https://climatedataguide.ucar.edu). To indicate Ekman downwelling/upwelling, wind stress curl (hereafter curl, N m^{-3}) was calculated from WS, UW, and VW following *Large and Pond* [1981]. Sea surface height anomaly (SSH, cm) which can be used to indicate basin-scale gyre intensity in the SCS

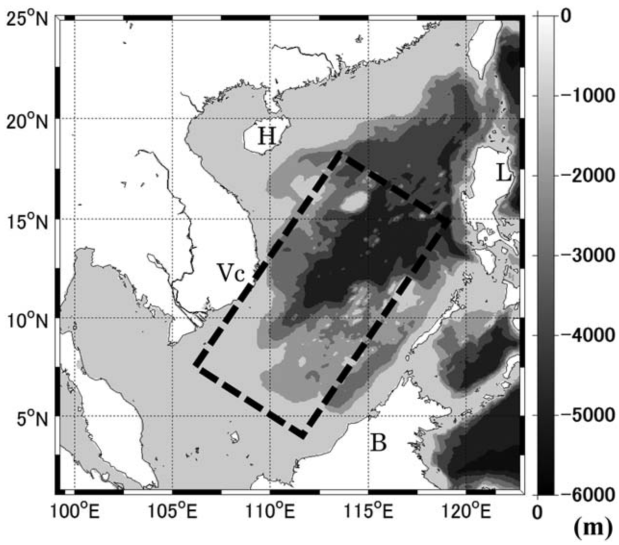

Figure 1. Map of South China Sea (SCS) showing bottom depth (as negative values). A black dashed rectangle borders the area for which the time series of mean Chl *a* (shown in Figure 3) was derived. The labels Vc, H, L, and B indicate the Vietnamese coast, Hainan Island, Luzon Island, and Borneo Island, respectively.

[e.g., *Wu and Chang*, 2005; *Chang et al*., 2008] was also investigated, using data acquired from the Copernicus Marine and Environmental Service (CMEMS, http://marine.copernicus.eu). Subsets of data over the region of study (Figure 1) were extracted from global-coverage satellite and reanalyzed data. The study region encompassed latitudes from 1°N to 25°N and longitudes from 99°E to 123°E, and included shallow waters (bottom depths > -200 m, where negative values indicate below the sea surface) and the SCS deep basin (bottom depths < -5000 m).

2.2. Data Analysis

The spatiotemporal impacts of El Niño on biogeophysical variables were defined using data within the period of the SeaWiFS ocean color mission (i.e., September 1997 to December 2010). The reason for selecting this study period was to obtain results comparable to those of the above mentioned previous studies, which were based mainly on satellite Chl *a* data from that period.

Because our study focuses on the detailed spatiotemporal evolution (i.e., surface area changes and time lag) of the El Niño impacts relating to biogeophysical variables, our data analysis focused on the linear regression of biogeophysical variables against the El Niño index using different time lags (correlations with a lead or lag by El Niño). The monthly anomaly of SST in the Nino3.4 region, acquired from the US National Oceanographic and Atmospheric Administration (NOAA) Climate Prediction Center (http://www.cpc.ncep.noaa.gov/data/indices/sstoi.indices), was used as the El Niño index (hereafter called Nino3.4). To avoid interference from seasonal signals on El Niño-related biogeophysical variability, we used the anomalies of all biogeophysical variables (i.e., the departure from the mean monthly climatological variables) followed by detrending of the variables. We neither explicitly express "anomalies" nor use the specific nomenclature for anomaly values of biogeophysical variables. Hereafter, for instance, we use "Chl *a*" interchangeably to refer to Chl *a* in general terms and also specifically when we discuss the results of our analysis based on Chl *a* anomaly data; the same convention is used for the other geophysical variables.

We applied multiple linear regression of standardized Chl *a* to standardized SST, MLD, and PAR to approximately determine the limiting factors for phytoplankton in the SCS during different seasons; i.e., northeast monsoon/boreal winter (December–January–February), first monsoon transition period/boreal spring (March–April–May), southwest monsoon/boreal summer (June–July–August), and second monsoon transition period/boreal fall (September–October–November). Prior to the regression analysis, all variables were standardized (mean = 0 and standard deviation = 1) using a *Z*-score transformation [e.g., *Nathans et al*., 2012; *Siswanto et al*., 2016a], so that the partial regression weights for SST (β_{SST}), MLD (β_{MLD}), and PAR (β_{PAR}) also reflected the corresponding relative importance of SST, MLD, and PAR in determining Chl *a* variability.

Ocean color and infrared sensor-retrieved data can contain gaps due to cloud cover and rain belts. Although correlations between Nino3.4 and biogeophysical data containing spatiotemporal gaps can be derived, the correlation (and hence the El Niño impact) in one pixel is statistically incompatible with those in other pixels, because the pixels have different degrees of freedom. Therefore, prior to removing the seasonal signal and detrending each variable, we applied a Data Interpolating Empirical Orthogonal Function (DINEOF) technique to construct spatiotemporally complete SeaWiFS Chl *a*, SeaWiFS PAR, AVHRR SST, and MODIS SST data sets. DINEOF was not applied to WS, UW, VW, MLD, RR, and SSH because there were no spatiotemporal gaps in those data sets. Previous studies showed that DINEOF is effective in filling spatiotemporal gaps in satellite data [e.g., *Alvera-Azcárate et al*., 2005; *Siswanto et al*., 2016a].

3. Results

3.1. Limiting Factors for Phytoplankton in the SCS

Previous studies suggest that phytoplankton in the SCS are limited by nutrient resources [e.g., *Wu et al*., 2003; *Chen et al*., 2004; *Tang et al*., 2004]. However, the detailed spatial features of phytoplankton sensitivity to nutrients have not been identified. Identifying the specific areas of the SCS where phytoplankton are more limited by nutrient resources is a prerequisite to understanding the mechanisms underlying Chl *a* variability in the SCS, in terms of more detailed spatial features relating to El Niño.

Figure 2 shows pixel-based multiple linear regression results for the determination coefficient (R^2, first column), β_{SST} (second column), β_{MLD} (third column), and β_{PAR} (fourth column) in different seasons. It can be clearly seen that SST exhibits the strongest correlation with Chl *a*, as depicted by large negative β_{SST} (Figures 2b, 2f, 2j, and 2n), whose spatial patterns resemble those of high R^2 of about $>$0.5 (Figures 2a, 2e, 2i, and 2m). Negative β_{SST} indicates that surface cooling is associated with an increase in Chl *a*, as surface cooling is usually associated with an increase in nutrients caused by physical processes (e.g., vertical mixing and upwelling), and therefore implies that phytoplankton in the SCS are more limited by nutrient versus light availability. Positive β_{MLD} (Figures 2c, 2g, 2k, and 2o), except in the center of the SCS, also suggests an effect of limited nutrient availability on Chl *a* (i.e., increase in wind-driven vertical mixing increases nutrients to increase Chl *a*).

Negative β_{MLD} over the center of the SCS indicates a decrease in Chl *a* when MLD deepens, which implies that the nutrient availability determining Chl *a* variability in the center of the SCS is more controlled by wind-driven Ekman convergence/divergence than by wind-driven vertical mixing. Negative, and less remarkable positive β_{PAR} (Figures 2d, 2h, 2l, and 2p) compared with marked negative β_{SST}, indicates that light is less important than nutrients for limiting phytoplankton growth.

The time series of mean Chl *a* averaged over the central basin of the SCS (bounded by a black dashed rectangle in Figure 1), which is approximately out of phase with that of mean SST (Figure 3), also indicates the importance of nutrient resources in determining Chl *a* variability. It is apparent that there was high Chl *a* accompanied by low SST in the summer before the mature phase of El Niño (notably in June–September 2002 and June–September 2009), and low Chl *a* with high SST in the summer after the mature phase of El Niño (in particular, June–September 1998, July–September 2007, and June–September 2010).

We analyzed separately the total and anomaly values of Chl *a* and SST data from all summers before the mature phase, all winters during the mature phase, and all summers after the mature phase of El Niño. In the central basin of the SCS, higher Chl *a* in the summer before the El Niño mature phase was observed in terms of total Chl *a*, compared with the summer after the mature phase (Figures 4a and 4c); this difference is more obvious in Chl *a* anomaly data (Figures 4d and 4f). In terms of both total (Figures 5a and 5c) and anomaly data (Figures 5d and 5f), SST was lower in the summer before the El Niño mature phase compared with the summer after the mature phase. As will be detailed in the following sections, high Chl *a* and low SST were observed in the summer before the mature phase of El Niño. The opposite conditions in the summer after the mature phase of El Niño are related to reversals of the SCS basin-scale circulation and surface ocean jet off the Vietnamese coast. *Chang et al*. [2008] showed that the summer ocean circulation reversal is stronger during El Niño Modoki than during canonical El Niño events.

Low Chl *a* and high SST were also observed during the mature phase of El Niño (notably in December 1997 to February 1998, November 2002 to January 2003, and January–February 2010). On the other hand, the impacts of the El Niño mature phase, which include low Chl *a* and an increase in total SST (Figures 4b and 5b), were hidden by seasonal variations. Low Chl *a* and high SST in winter during the El Niño mature phase were visible in anomaly data (Figures 4e and 5e). As will be detailed below, such low Chl *a* is ascribed to weakening cyclonic ocean surface circulation in winter due to a weakening northeast Asian monsoon during the mature phase of El Niño [e.g., *Wu and Chang*, 2005; *Chang et al*., 2008; *Lan et al*., 2012]. Two consecutive positive SST peaks, one during the mature phase and the other one during the summer after the mature phase of El Niño, have been noted in other studies [e.g., *Xie et al*., 2003; *Wang et al*., 2006], but the accompanying negative peaks of Chl *a* have not been reported

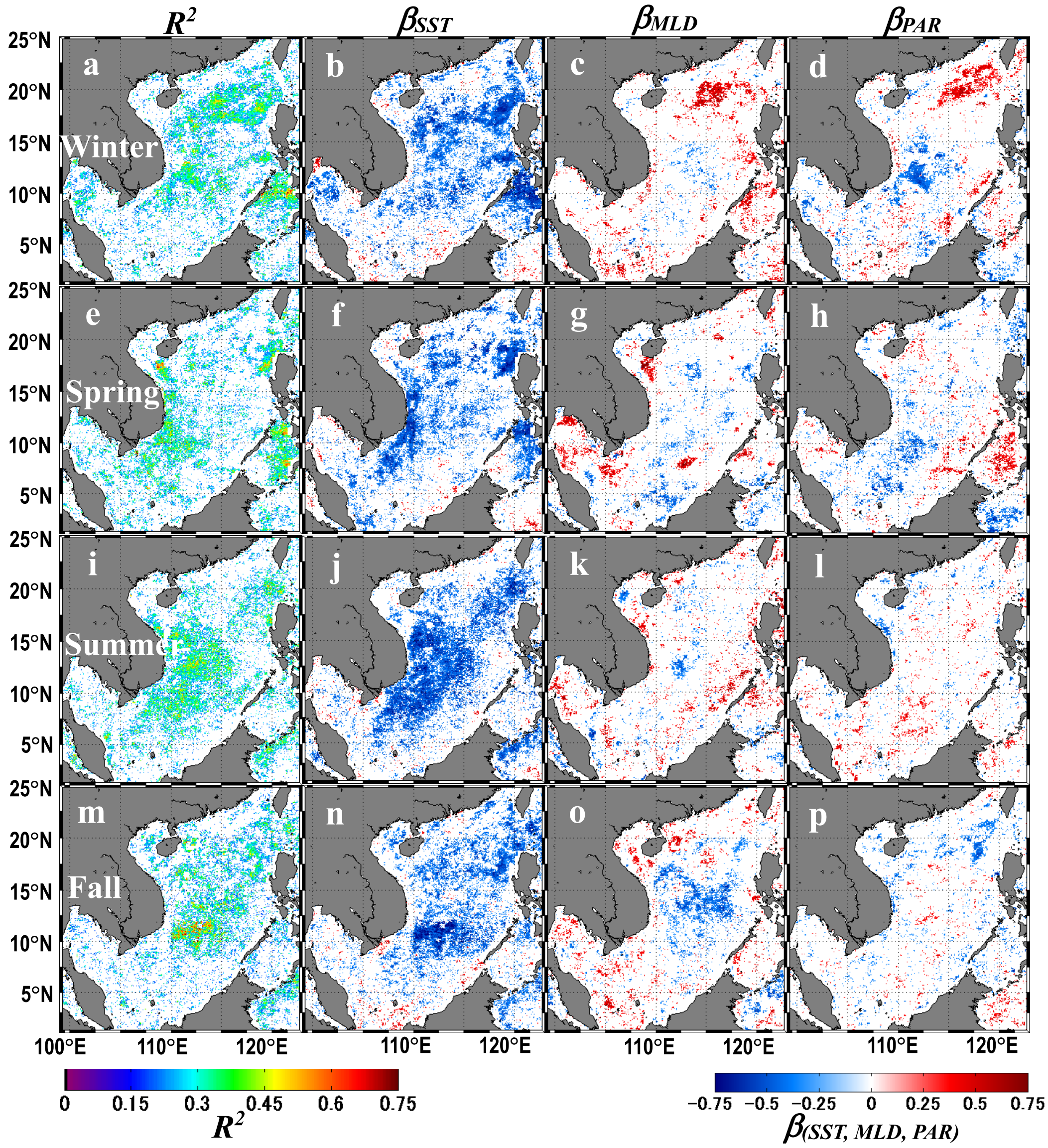

Figure 2. Spatial variations of significant ($p < 0.05$) (a) determination coefficients (R^2), standardized partial regression coefficients for (b) SST (β_{SST}), (c) MLD (β_{MLD}), and (d) PAR (β_{PAR}) for winter (December–January–February) from multiple linear regression analysis. Areas with insignificant R^2, β_{SST}, β_{MLD}, and β_{PAR} are masked out (white areas). (e–h, i–l, m–p) The same as Figures 2a–2d, except that the analyses were conducted for spring (March–April–May), summer (June–July–August), and fall (September–October–November), respectively.

previously. As will be described below, different geophysical processes during El Niño developing and mature phases (although Nino3.4 is positive) lead asymmetrical Chl *a* and SST oscillations with respect to Nino3.4.

Whether canonical El Niño and El Niño Modoki are different types of El Niño is still under debate [see *Ashok et al.*, 2007; *Takahashi et al.*, 2011; *Karnauskas*, 2013; *Marathe et al.*, 2015]. We therefore focused our analysis only on the general category of El Niño, and thus used Nino3.4 (which encompasses both El Niño types), instead of Nino3 (which captures mainly canonical El Niño events) or the El Niño Modoki index. We describe the biogeophysical impacts from the viewpoint of El Niño (positive Nino3.4), because previous studies investigated the spatiotemporal variability of Chl *a* associated with El Niño [e.g., *Zhao and Tang*, 2007; *Palacz et al.*, 2011; *Liao et al.*, 2012]; this also allows us to compare our results with those of previous studies.

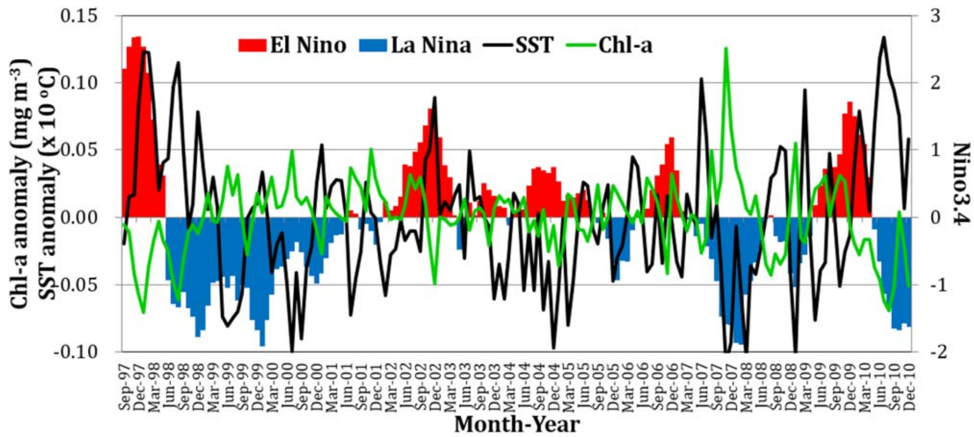

Figure 3. (a) Time series of mean Chl *a* (green line), mean SST (black line), and Nino3.4 indicating El Niño (red bar) and La Niña (blue bar) phases for the period from September 1997 to December 2010. Chl *a* and SST were derived from the area bordered by a black dashed rectangle in Figure 1.

3.2. Detailed Spatiotemporal Impacts of El Niño on Phytoplankton Biomass and Underlying Atmosphere-Ocean Physical Interactions in the SCS

Asymmetric temporal variation in Chl *a* values with respect to Nino3.4 indicates that El Niño may lead or lag Chl *a* changes in the central basin of the SCS (Figures 3–5). However, it remains unclear whether Chl *a* over the entire SCS basin (including coastal areas) exhibits similar Chl *a* temporal evolution. Figures 6–8 show the detailed spatiotemporal evolutions of biogeophysical variables with respect to El Niño, as indexed by the coefficient of correlation (r) between Nino3.4 and variables at different time lags. With respect to

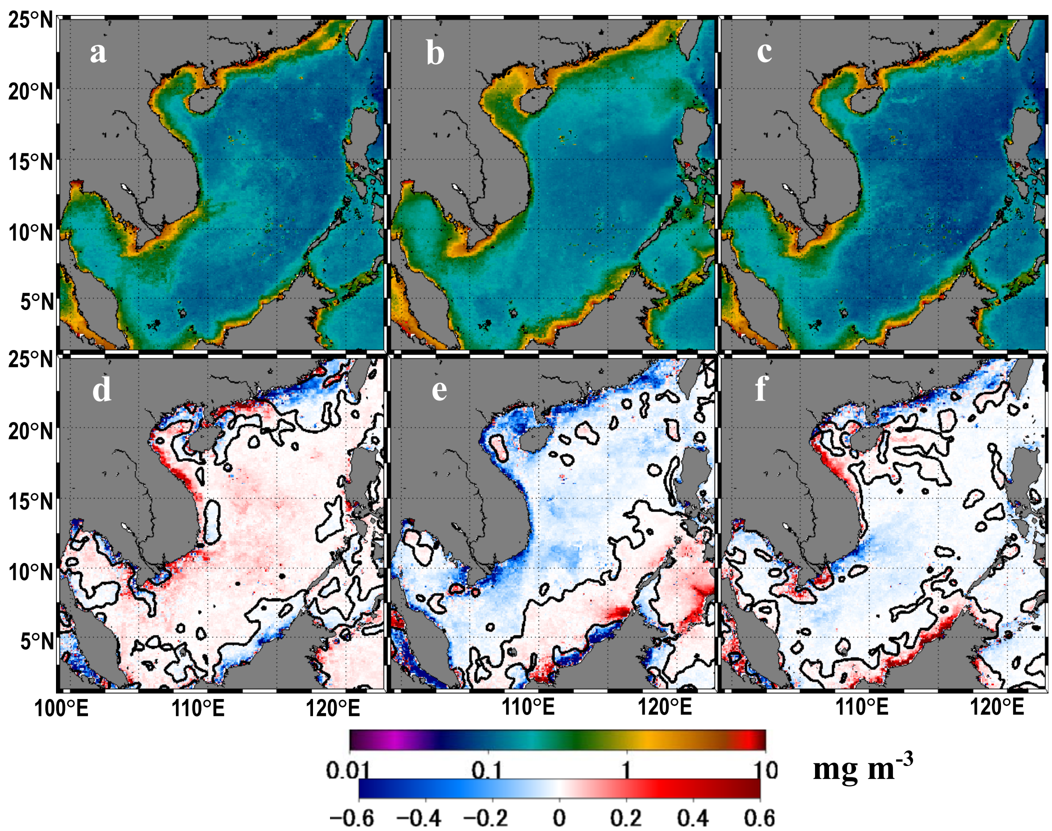

Figure 4. Mean Chl *a* (a) in the summer before the El Niño mature phase, (b) in winter during the El Niño mature phase, and (c) in the summer after the El Niño mature phase. (d–f) The same as Figures 4a–4c, but present the mean Chl *a* anomaly field.

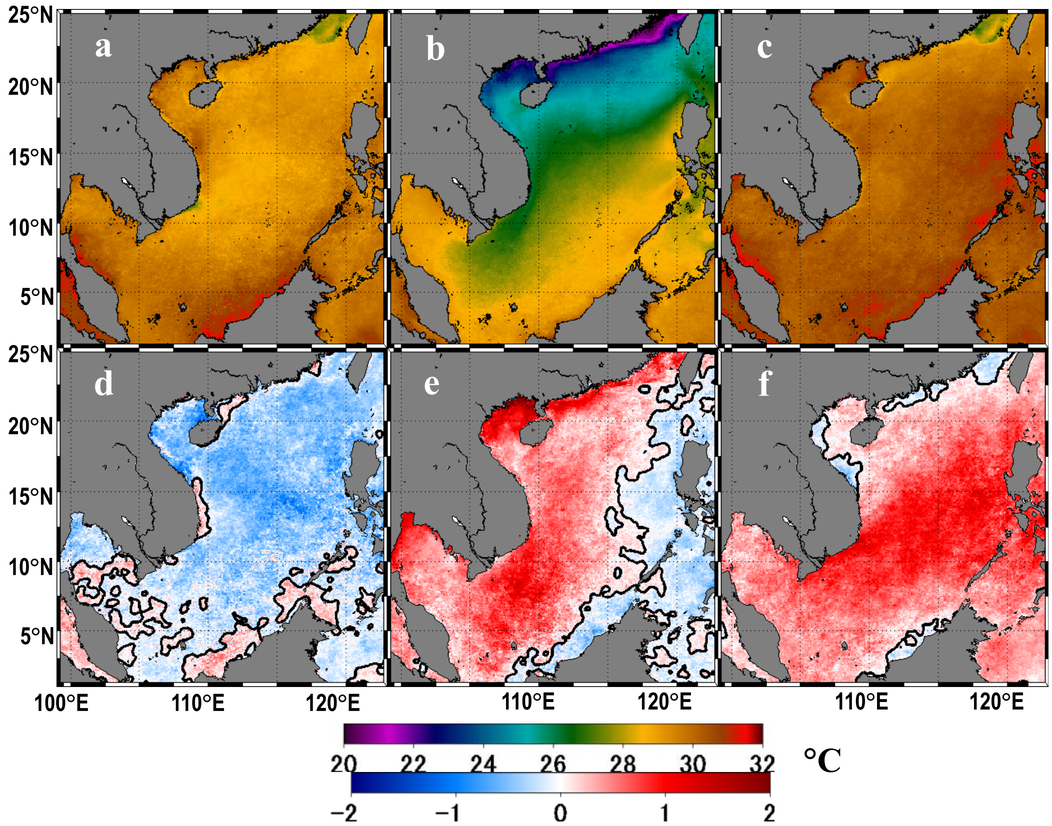

Figure 5. As described in Figure 4, but presents (a–c) mean SST and (d–f) mean SST anomaly.

positive Nino3.4 results, blue (red) areas indicate low (high) Chl *a* (Figures 6a–6g), SST (Figures 6h–6n), WS (Figures 7a–7g), MLD (Figures 7o–7u), SSH (Figures 7v–7z2), and RR (Figures 8a–8g) values. The blue (red) areas on VW (Figures 6o–6u) and UW plots (Figures 6v–6z2) indicate northerly (southerly) and easterly (westerly) wind components, respectively. The blue (red) areas for curl (Figures 7h–7n) indicate Ekman convergence (Ekman divergence). Vectors in Figures 7a–7g represent *r* values for Nino3.4 versus VW (Figures 6o–6u) and Nino3.4 versus UW (Figures 6v–6z2) maps. The vector length does not indicate magnitude, but a tendency to a certain wind direction. Negative (–) lag in Figures 6–8 refers to a lead by the time series of the biogeophysical variables, whereas positive (+) lag refers to a lead by the Nino3.4values. A 0 month lag is considered as the footprint of the mature phase of El Niño, and normally occurs during winter [e.g., *Wu and Chang*, 2005].

In general, the biogeophysical evolution within the period spanning the El Niño developing phase (−6 month lag) to post-El Niño (+6 month lag) in the SCS can be described as follows: (1) basin-scale high Chl *a* changes to basin-scale low Chl *a* (Figures 6a–6g); (2) basin-scale low SST changes to basin-scale high SST (Figures 6h–6n); (3) VW in the northern (southern) basin tends to be more dominated by southerly (northerly) winds (Figures 6o–6u); (4) UW in the northern (southern) basin tends to be more dominated by westerly (easterly) winds (Figures 6v–6z2); (5) during the developing phase, anticyclonic (cyclonic) wind circulation is formed between the Vietnamese coast and Borneo Island (between Hainan Island and Luzon Island) (Figures 7a and 7b); (6) the area of decreased (increased) WS in the northern (southern) basin expands (shrinks), accompanied by an expanding area of anticyclonic wind circulation originally formed between the Vietnamese coast and Borneo Island (Figures 7a–7g); (7) the central SCS basin tends to be more dominated by negative curl (Ekman convergence) (Figures 7h–7n); (8) the area of increased MLD between the Vietnamese coast and Borneo Island expands (Figures 7o–7u), accompanied by a strengthened positive SSH (Figures 7v–7z2); and (9) high RR over the Mekong River basin and northern Borneo Island tends to reduce (Figures 8a–8g). Below, we describe the detailed spatiotemporal changes in Chl *a* and the underlying geophysical factors within the three phases, i.e., during developing, mature, and weakening El Niño phases.

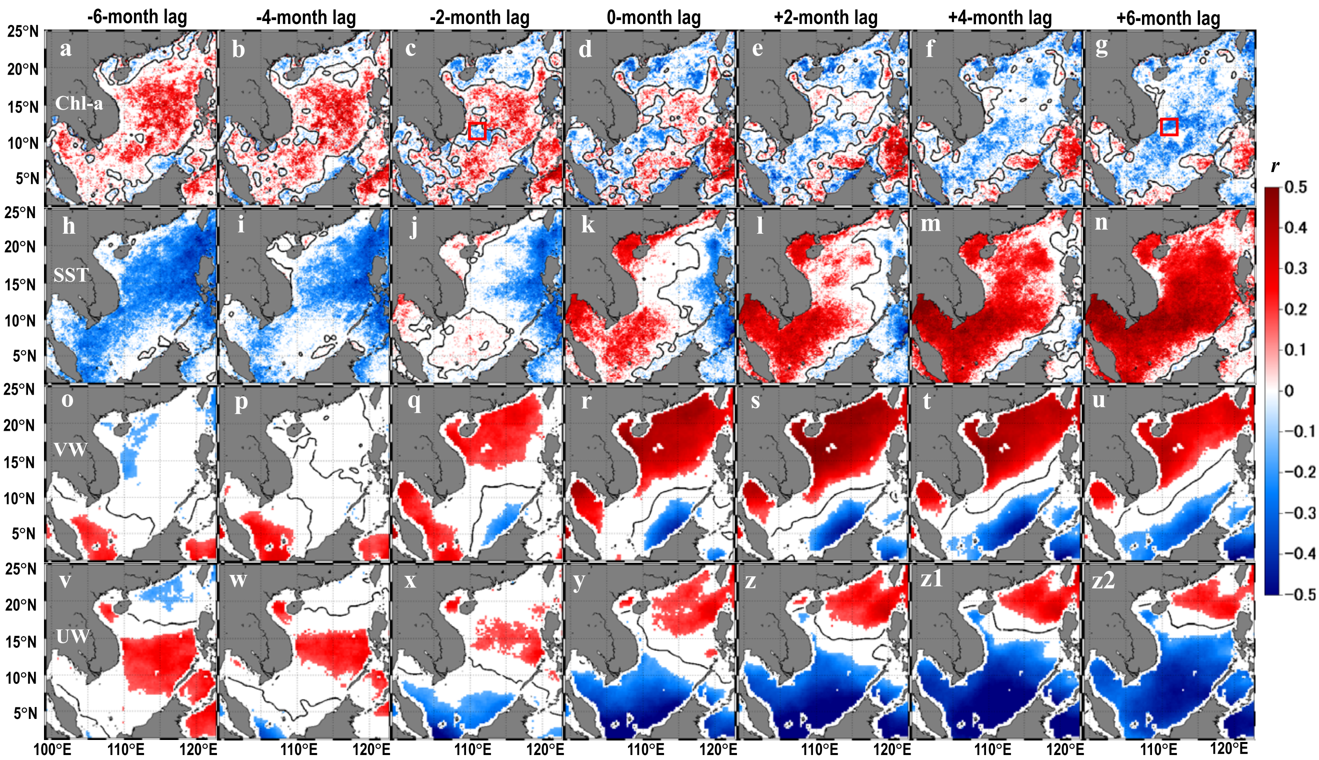

Figure 6. Spatial variations of correlation coefficients (r) derived from regressions of Chl *a* against Nino3.4 at (a) −6 month, (b) −4 month, (c) −2 month, (d) 0 month, (e) +2 month, (f) +4 month, and (g) +6 month lags (where negative (–) lag refers to a lead by variables, and positive (+) lag refers to a lead by Nino3.4). (h–n, o–u, v–z2) The same as Figures 6a–6g, except that values of r were derived from regressions of Nino3.4 against SST, VW, and UW, respectively. White areas and black lines indicate insignificant r ($p > 0.05$) and $r = 0$, respectively. The red box in Figures 6c and 6d aligns with Box S defined in *Zhao and Tang* [2007] and *Tan and Shi* [2009].

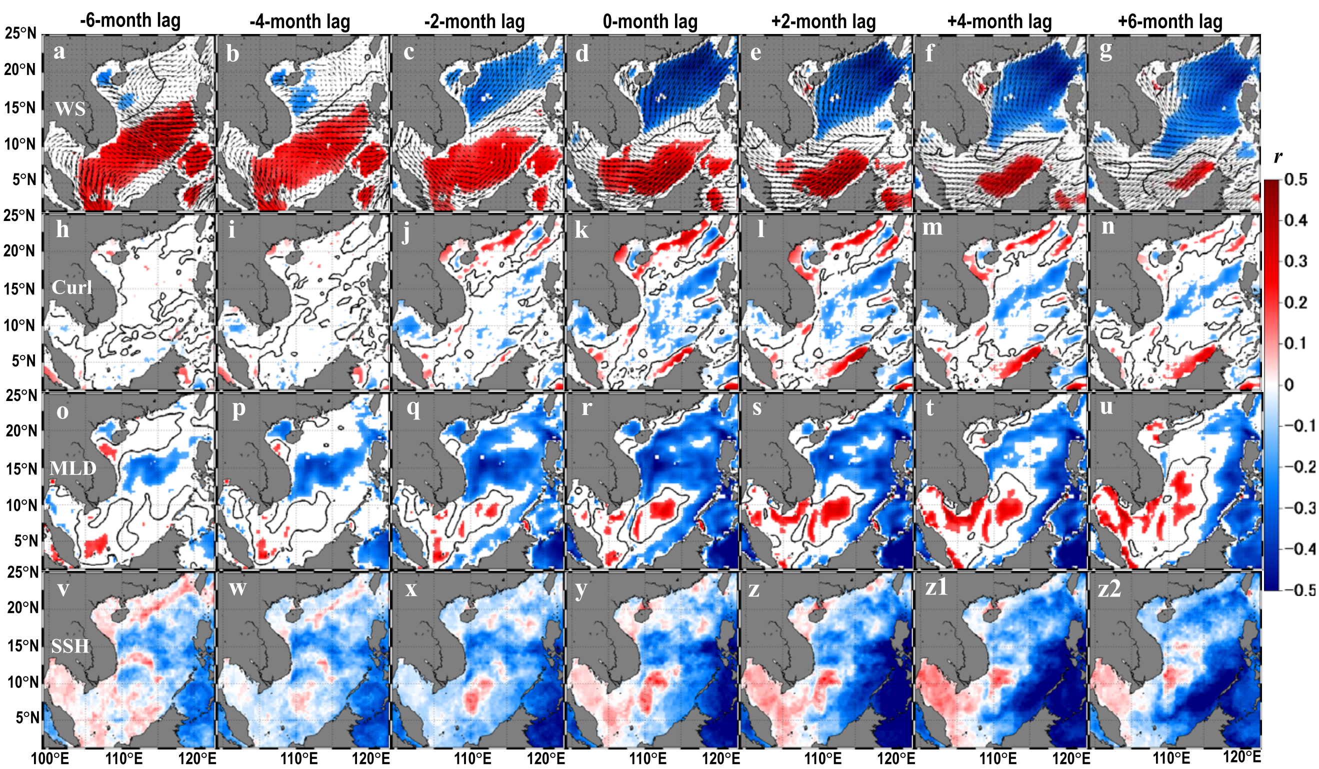

Figure 7. Same as Figure 6, except that values of r were derived from regressions of Nino3.4 against (a–g) WS, (h–n) curl, (o–u) MLD, and (v–z2) SSH. Note that both significant and insignificant r values are included in Figures 7v–7z2.

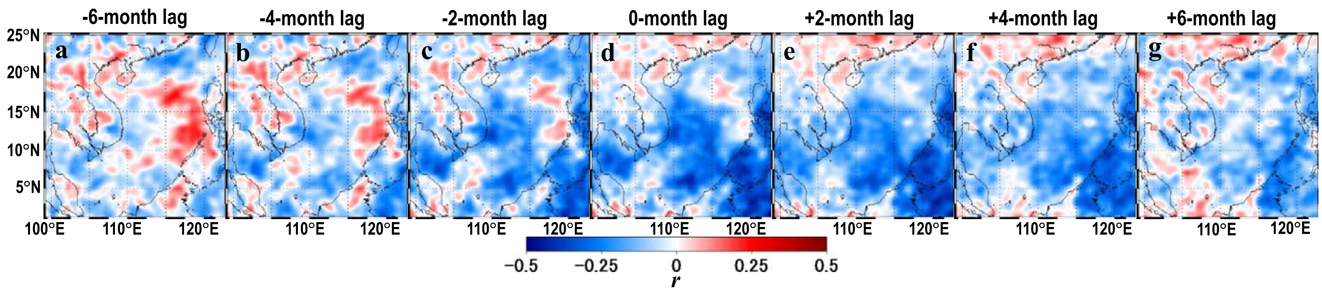

Figure 8. As described in Figures 6a–6g, except that values of *r* were derived from regression of Nino3.4 against RR. Note that both significant and insignificant *r* values are included.

3.2.1. Summer During the El Niño Developing Phase

High Chl *a* and low SST over the entire SCS basin (especially the northern basin) with a −6 to −4 month lag are apparent in our observations (Figures 6a, 6b and 6h, 6i). Considering the remarkably negative β_{SST} and weakly negative β_{MLD} values in summer (Figures 2j and 2k), the Chl *a* increase in the northern basin is likely caused by nutrient input from the deep layer without intense vertical mixing. High curl, shallow MLD, and low SSH in the northern basin (Figures 7h, 7i; 7o, 7p; and 7v, 7w) indicate that high Chl *a* in the northern basin is likely caused by an increase in nutrients supplied by Ekman divergence associated with a cyclonic wind circulation (Figures 7a and 7b).

High Chl *a* and low SST are also apparent in the southern basin. This basin is characterized by Ekman convergence, as indicated by anticyclonic wind circulation, negative curl, deep MLD, and high SSH (Figures 7a, 7b; 7h, 7i; 7o, 7p; and 7v, 7w). One possible mechanism underlying an increase in Chl *a* and decrease in SST is that strengthened WS leads to vertical entrainment of cold, nutrient-rich deep water. This mechanism is supported by the observation that summer β_{MLD} values are more often positive than negative, while negative β_{SST} values are more common (Figures 2j and 2k).

Strengthened WS with dominant westerly winds in the central SCS is associated with intense Asian summer monsoons during the developing phase of El Niño [e.g., *Chang et al.*, 2008]. *Chang et al.* [2008] further showed that these westerly winds belong to the western North Pacific summer monsoon (WNPSM) circulation, which also intensifies in summer during the developing phase of El Niño. The intense Asian summer monsoon is known to strengthen anticyclonic (cyclonic) ocean surface circulation in the southern (northern) basin [*Wu and Chang*, 2005; *Chang et al.*, 2008], as confirmed by positive (negative) SSH in the southern (northern) basin [see also *Chang et al.*, 2008, Figure 1a].

Strengthened anticyclonic (cyclonic) ocean surface circulation in the southern (northern) basin intensifies eastward surface flow and upwelling off the Vietnamese coast [*Chang et al.*, 2008]. Thus, cyclonic ocean and wind circulation in the northern basin, strengthened WS in the southern basin, and upwelling off the Vietnamese coast are the three primary mechanisms underlying the basin-scale Chl *a* increase (SST decrease) observed during the developing phase of El Niño.

Forced by anticyclonic wind circulation over the SCS southern basin between the Vietnamese coast and Borneo Island, SST increased in that region with a −2 month lag (Figure 6j); this increase was accompanied by a more marked negative curl, increased MLD, and high SSH (Figures 7j, 7q, and 7x). A clear decrease in Chl *a* was evident only along the southeast coast of Vietnam (Figure 6c), which contradicts the positive curl in this area (Figure 7j). Positive curl off the Vietnamese coast during the El Niño developing phase is also noted by *Wang et al.* [2006].

Low Chl *a* off the Vietnamese coast is likely due to a reduction in nutrients supplied by the Mekong River. Discharge from the Mekong River is an essential source of nutrients determining variability in Chl *a* east of the Vietnamese coast [e.g., *Tang et al.*, 2004]. This relationship is confirmed by the positive *r* values of the Mekong River discharge versus Chl *a* observed in the coastal region off Vietnam (Figure 9a). During an El Niño event, Mekong River discharge decreases due to drought across its watershed [*Rasanen and Kummu*, 2013]. In observations of the spatial variation of *r* between Nino3.4 and rain RR (Figure 8), RR over the Mekong River downstream basin began to decrease with a −2 month lag (Figure 8c), and the Mekong River discharge started to decline below normal before the mature phase of El Niño (Figure 10a).

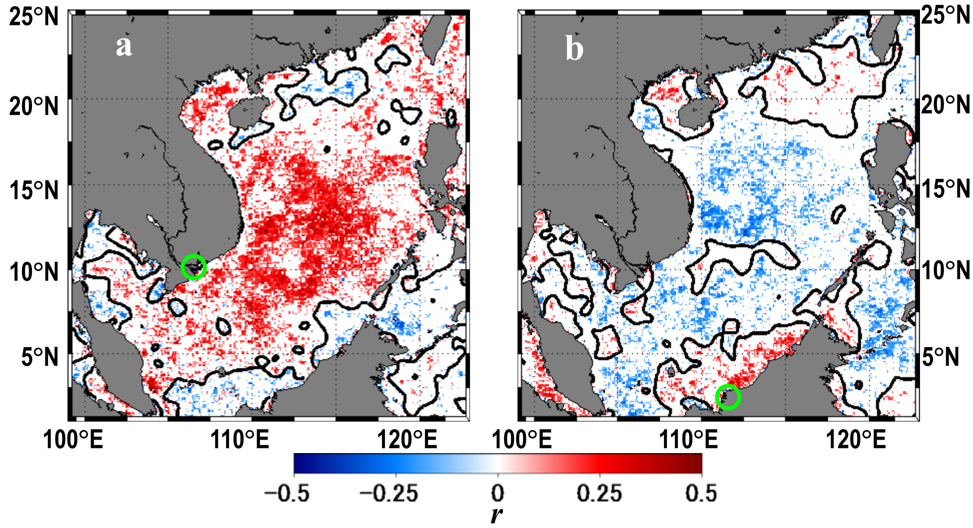

Figure 9. Spatial variations of correlation coefficients (r) derived from regressions of Chl *a* against (a) Mekong River discharge and (b) Rajang-Kapit Wharf River discharge with no time lag. White areas and black lines indicate insignificant r ($p > 0.05$) and $r = 0$, respectively. The green circles in Figures 9a and 9b indicate the approximate position of the Mekong River mouth and Rajang-Kapit Wharf River mouth, respectively.

A large area showing a decrease in Chl *a* with a −2 month lag (around fall) in the northern SCS was also observed. WS had already weakened significantly in the north with a −2 month lag (Figure 7c). Furthermore, VW and UW in the north were characterized by southerly and westerly winds, respectively (Figures 6q and 6x), thereby generating southwesterly alongshore winds (Figure 7c). Such alongshore winds lead to coastal upwelling, which was confirmed by a marked increase in curl in the northern coastal area (Figure 7j), as also reported by *Wang et al*. [2006] and *Yan et al*. [2015]. However, one may ask why upwelling does not increase Chl *a* in the northern coastal areas. High R^2 accompanied by a marked positive β_{MLD} and negative β_{SST} in the northern SCS in fall (Figures 2m–2o) indicates that vertical mixing largely determines nutrient supply from the deep layer. Therefore, weakened WS (Figure 7c) over the northern SCS basin in the fall before the mature phase of El Niño, which causes a decrease in MLD and thereby weakened vertical entrainment (Figure 7q), likely reduces nutrient supply from the deep layer and thus decreases Chl *a*.

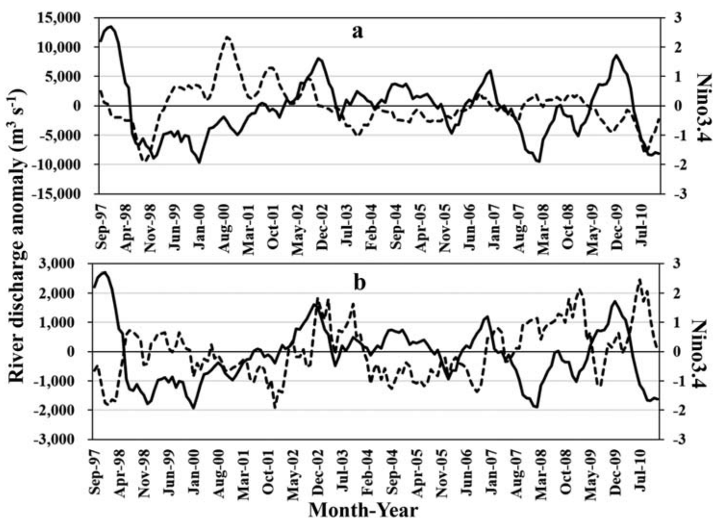

Figure 10. (a) Time series of Nino3.4 results (solid line) and 5 month moving average of Mekong River discharge (dashed line) for the period from September 1997 to December 2010. (b) The same as Figure 10a, except that the dashed line represents Rajang-Kapit Wharf River discharge.

3.2.2. Winter During the El Niño Mature Phase (∼0 Month Lag)

Cyclonic wind circulation in the northern basin and anticyclonic wind circulation between the Vietnamese coast and Borneo Island that formed during the developing phase had completely disappeared by the 0 month lag (Figure 7d). Basin-scale wind circulation tends to be anticyclonic in the eastern SCS, which is consistent with *Lan et al.*'s [2012] and *Yan et al.*'s [2015] findings, and is caused by weakened northeasterly Asian monsoon winds during the mature phase [*Wu and Chang*, 2005; *Chang et al.*, 2008; *Lan et al.*, 2012].

Lan et al. [2012] further observed that such anticyclonic wind circulation drives anticyclonic ocean surface circulation, especially in the area between Vietnam and Borneo Island. This anticyclonic ocean surface circulation is consistent with observed increases in MLD and SSH (Figures 7r and 7y), reflecting more intense Ekman convergence. Therefore, besides the tendency toward decreased Mekong River discharge, a tendency for more intense Ekman convergence may also contribute to the large, well-defined areas of low Chl *a* and high SST southeast of Vietnam during a mature El Niño (Figures 6d and 6k). Such a Chl *a* spatial pattern during 0 month lag largely resembles that reported by *Liao et al.* [2012] who suggested it was caused by El Niño Modoki.

Low Chl *a* along the northern coast also becomes more well-defined under these conditions, while positive curl becomes more marked due to a long-lasting northeastward alongshore wind [see also *Jing et al.*, 2011]. This enlarged area of low Chl *a* is likely caused by a markedly weakened WS, considering that Chl *a* variability during winter is largely controlled by MLD variability (see the highly positive β_{MLD} in Figure 2c). Notable positive curl was also observed along the northwest coast of Borneo Island (Figure 7k), reflecting strengthened winter upwelling, which was confirmed by the presence of SST cooling (Figure 6k) [see also *Yan et al.*, 2015; *Sun*, 2017]. Effect of upwelling to increase nutrient supply from deeper layer was strong in the northernmost tip of Borneo Island as indicated by prominent Chl *a* increase and SST decrease, which is consistent with *Yan et al.*'s [2015] result.

In contrast, Chl *a* along the northeastern coast of Borneo was consistently low, meaning that processes other than upwelling control nutrient levels. RR over northern Borneo Island decreased during the El Niño mature phase (Figure 8d). This observation is consistent with Rajang-Kapit Wharf River discharge (representing total river discharge in the northern Borneo Island), which is relatively low during the mature phase of El Niño (Figure 10b). Decreasing RR (hence river discharge) reduces nutrient input from rivers. This finding is supported by a strong positive *r* between Rajang-Kapit Wharf River discharge and Chl *a* along the northwestern coast of Borneo Island (Figure 9b), meaning that high (low) input of nutrients from rivers will increase (decrease) Chl *a*. Our results are consistent with *Sun*'s [2017] work suggesting that nutrient discharge from rivers is more important than upwelling caused by northeasterly winds in determining interannual Chl *a* variability along the northwestern coast of Borneo Island.

3.2.3. Summer During the El Niño Weakening Phase

Entering the weakening phase of El Niño, basin-scale anticyclonic wind circulation was still present, with steadily decreasing WS (Figures 7e–7g), which led to weakened basin-scale WS with a +8 month lag (roughly in summer, Figure 11a) when anomalous easterly winds prevail over the central basin [see also *Chang et al.*, 2008; *Wang et al.*, 2006; *Jing et al.*, 2011; *Lan et al.*, 2012]. *Chang et al.* [2008] found that these easterly winds in the central SCS belong to WNPSM circulation, which flows strongly westward in summer during the El Niño weakening phase. This easterly (onshore) wind drives cyclonic (anticyclonic) ocean circulation in the southern (northern) basin along with a shoreward surface current, resulting in diminished upwelling off the Vietnamese coast compared with a normal summer season [e.g., *Wu and Chang*, 2005; *Lan et al.*, 2012].

This study presents the first detailed temporal analysis of wind circulation over the center of the SCS. We observed a shift from westerlies during the developing phase to easterlies during the weakening phase of El Niño, which is related to the WNPSM circulation reversal [*Chang et al.*, 2008]. In terms of ocean circulation, this study suggests a detailed transition from anticyclonic during the El Niño developing phase to cyclonic during the weakening phase in the southern basin, with a complementary shift from cyclonic to anticyclonic in the northern basin. This pattern can also be expressed as a northeastward shift in the anticyclonic ocean surface circulation from the southern to northern basin during the evolution of an El Niño event.

Northeastward shifts of negative curl observations (Figures 7l–7n and 11b), deep MLD (Figures 7s–7u and 11c) and high SSH (Figures 7z–7z2 and 11d) within the period from the El Niño mature phase to summer (+8 month lag) reflect the northeastward shift of anticyclonic ocean circulation. In particular, the distribution of SSH at +8 month lag (Figure 11d), i.e., high SSH extending from the east of Vietnam to northwest of Luzon Island and low SSH in the southern, eastern, and northern SCS, resembles the pattern during summer 1998 reported by *Wu and Chang* [2005] (see their Figure 4c). This SSH feature is clearly associated with cyclonic circulation in the southern basin and anticyclonic circulation extending from the Vietnamese coast to the area northwest of Luzon Island, as noted by *Lan et al.* [2012].

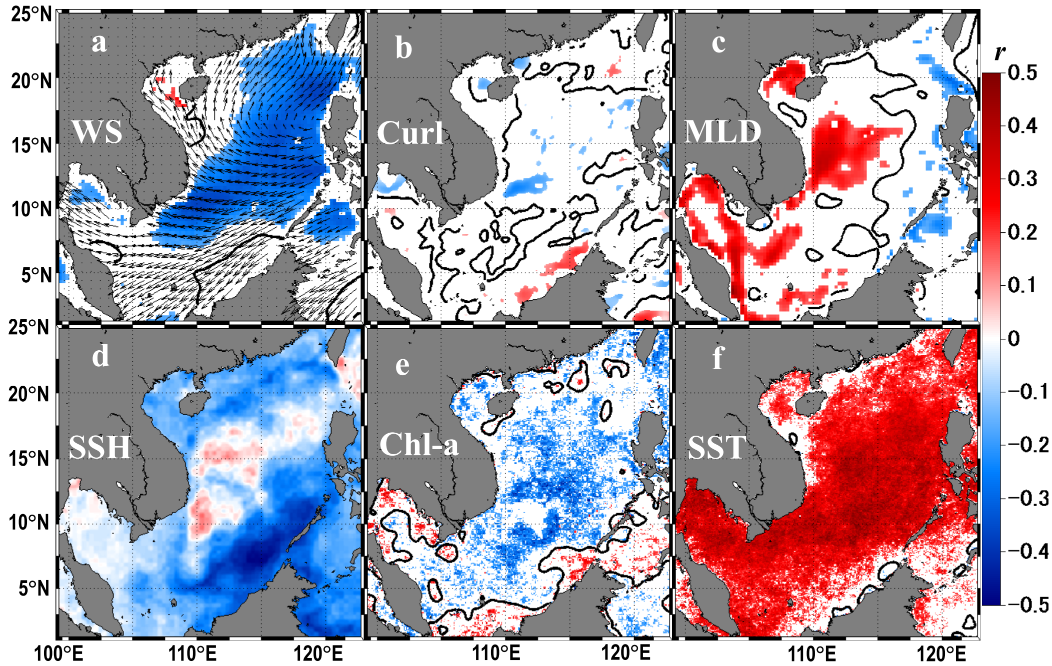

Figure 11. Spatial variations of correlation coefficients (r) derived from regressions of Nino3.4 against (a) WS, (b) curl, (c) MLD, (d) SSH, (e) Chl *a*, and (f) SST at +8 month lag. Vectors in Figure 11a indicate a tendency toward a certain wind direction. White areas and black lines indicate insignificant r ($p > 0.05$) and $r = 0$, respectively. Note that for SSH (Figure 11d), both significant and insignificant r values are included.

The combination of the aforementioned post-El Niño geophysical changes, i.e., basin-scale weakening of WS, northeastward shift of anticyclonic ocean circulation, and diminished upwelling off Vietnam, which collectively restrict vertical flux of cold nutrient-rich deep water, are thus responsible for maintaining basin-wide low Chl *a* (high SST) until summer (Figures 6e–6g; 6l–6n; and 11e, 11f). Note that the increase in MLD does not imply an entrainment of nutrients, as it is not due to active vertical mixing, but to Ekman convergence associated with anticyclonic ocean circulation. In section 4, we compare the spatiotemporal Chl *a* changes after the El Niño mature phase observed in this study with those previously reported by *Zhao and Tang* [2007], *Tan and Shi* [2009], and *Liao et al*. [2012], who suggested that the Chl *a* pattern observed after the El Niño mature phase is related to a canonical El Niño event.

4. Discussion

Zhao and Tang [2007] and *Tan and Shi* [2009] demonstrated a marked decrease in Chl *a* and primary productivity, respectively, east of the Vietnamese coast in summer 1998, as illustrated in Box S (see black box in their figures or red box in Figure 6g in this paper). Our study provides new information showing that a clear decrease in Chl *a* east of the Vietnamese coast is already observed with a 0 month lag (approximately in winter; Figure 6d), or even 2 months earlier before the mature phase of El Niño (−2 month lag; Figure 6c). Therefore, the decrease in Chl *a* east of the Vietnamese coast in June 1998 reported by *Zhao and Tang* [2007] and *Tan and Shi* [2009] not only is an independent local biophysical interaction (i.e., diminished upwelling off Vietnam that decreases nutrient supply, and thus decreases Chl *a*) but also forms part of a basin-scale decrease in Chl *a* that can be ascribed to a basin-scale anticyclonic wind circulation and decrease in Mekong River discharge.

Based on EOF analysis, *Liao et al*. [2012] reported a decrease in primary productivity (hereafter also referred to as Chl *a*) over the entire SCS basin, with more pronounced decreases east of the Vietnamese coast and northwest of Luzon Island (see their Figure 1a). They also suggested that this spatial pattern of Chl *a* is associated with the first mode of EOF (EOF-1) and is closely related to canonical El Niño at a +4 month lag, which is defined as the highest temporally lagged r between the time series of EOF-1 and the El Niño index in the Nino3 region, which primarily identifies canonical El Niño patterns.

Although we used Nino3.4 (including both canonical El Niño and El Niño Modoki), we also observed a basin-scale decrease in Chl *a* with more marked decreases east of the Vietnamese coast and northwest of Luzon Island at a +4 month lag (Figure 6f). In addition, the sharp decreases in Chl *a* appeared with a 0 month lag, during the period of El Niño mature phase in the winter (Figure 6d). Pronounced low Chl *a* northwest of Luzon Island indicates a reduction of nutrient supply from deeper waters. We suggest that a continual weakening of WS weakens wind-driven upwelling and vertical mixing (thereby decreasing nutrient supply and Chl *a*), because nutrients supplied by wind-driven upwelling and vertical mixing are responsible for the Chl *a* bloom northwest of Luzon Island during the winter [e.g., *Wang et al*., 2010]. Perhaps, as suggested by *Liao et al*. [2012], this low Chl *a* pattern will be more pronounced during canonical El Niño, as anomalous ocean dynamics in the SCS during the winter are more strongly affected by canonical El Niño [*Wu and Chang*, 2005].

Liao et al. [2012] also suggested that the second mode of EOF (EOF-2) characterized by increases in Chl *a* in the central and eastern SCS (see their Figure 1c) is highly correlated with El Niño Modoki with no time lag. Such a Chl *a* impact is almost identical to our results, which also show anomalously high Chl *a* in the central and eastern SCS with a −2 month lag (Figure 6c) or with no time lag (Figure 6d). However, the high Chl *a* values observed over the central and eastern SCS are likely remnants of basin-scale high Chl *a* during the El Niño developing phase (Figures 6a and 6b), which is expected to be more pronounced during El Niño Modoki, as anomalous atmosphere and ocean dynamics in the SCS during the El Niño developing phase are more strongly affected by El Niño Modoki [*Wu and Chang*, 2005; *Chang et al*., 2008].

The spatiotemporal changes in Chl *a* east of the Vietnamese coast noted by *Zhao and Tang* [2007], changes in Chl *a* over the entire SCS basin reported by *Liao et al*. [2012], and changes in geophysical variables observed by *Wu and Chang* [2005], *Chang et al*. [2008], *Lan et al*. [2012], and *Yan et al*. [2015] are all represented in this work. However, such biogeophysical changes throughout the SCS basin from the El Niño developing phase to the El Niño weakening phase likely reflect a mix of biogeophysical responses to both El Niño types, due to our use of Nino3.4, which captures both canonical El Niño and El Niño Modoki signals.

Regardless of the debate over whether canonical El Niño and El Niño Modoki differ or fall along a continuum of types [see *Ashok et al*., 2007; *Takahashi et al*., 2011; *Karnauskas*, 2013; *Marathe et al*., 2015], the SCS atmospheric and oceanic geophysical responses to eastern Pacific warming differ from responses to central Pacific warming [*Wu and Chang*, 2005; *Chang et al*., 2008; *Liao et al*., 2012]. To differentiate the detailed spatiotemporal evolution in Chl *a* and its underlying geophysical factors solely related to canonical El Niño or El Niño Modoki, it is necessary to separate data sets with eastern Pacific warming (e.g., 1997 typical canonical El Niño) from those with central Pacific warming (e.g., 2004 typical El Niño Modoki), excluding seemingly mixed El Niño events (e.g., 2002 and 2009 El Niños).

There have been few distinct canonical El Niño and El Niño Modoki within the period of modern ocean color observations. Thus, it is best to assimilate satellite-based Chl *a* data into a coupled atmosphere-marine ecosystem model [e.g., *Aita et al*., 2007; *Gregg*, 2008] to generate Chl *a* data sets over a decadal time scale.

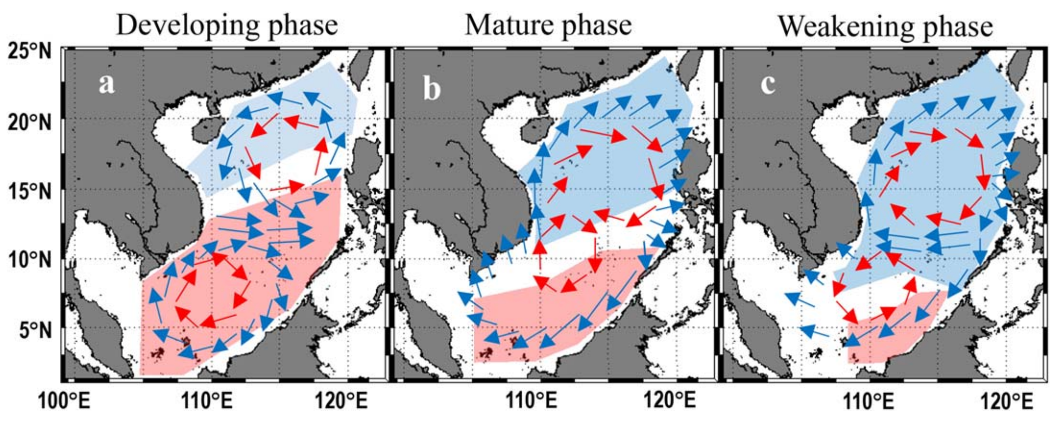

Figure 12. Simplified illustration of wind and ocean surface circulation underlying basin-scale Chl *a* and SST changes during the three main phases of El Niño: (a) developing, (b) mature, and (c) weakening. Blue and red arrows illustrate wind and ocean surface circulation, respectively. Blue and red shaded areas represent the regions exhibiting weakened and strengthened WS, respectively.

Then, by associating biogeophysical data sets with central Pacific warming to the El Niño Modoki index and those with eastern Pacific warming to Nino3, the footprints of different types of El Niño on the SCS biogeophysical environment can be elucidated.

5. Summary

With respect to El Niño evolution, atmosphere-ocean biogeophysical interactions in the SCS can be simplified into three El Niño phases, as illustrated in Figure 12, where the blue arrow indicates wind direction and the red arrow represents ocean circulation. During the developing phase of El Niño (Figure 12a), strengthened WNPSM circulation strengthens the Asian summer monsoon and drives intensified westerly winds over the central SCS; these winds enhance upwelling off Vietnam and drive cyclonic wind and ocean circulation in the northern basin. Thus, cyclonic ocean circulation in the northern basin, increased WS in the southern basin, and strengthened upwelling are together responsible for basin-wide high Chl *a* values due to entrainment of deep, nutrient-rich water, as indicated by low basin-wide SST. The initial decline of Chl *a* off the Vietnamese coast is ascribed to declining nutrient load from the Mekong River. During the El Niño mature phase (Figure 12b), a weakened Asian winter monsoon leads to anticyclonic wind and ocean circulation. This anticyclonic circulation broadens the low Chl *a*, high SST area in the northern and western SCS. A well-defined low Chl *a* area northwest of Luzon Island may be ascribed to decreased nutrient entrainment due to weakened wind-driven upwelling and vertical mixing. Low Chl *a* observed along the northwestern coast of Borneo Island is likely associated with declining nutrient supply caused by a decrease in river discharge. During the El Niño weakening phase (Figure 12c), weakened WNPSM circulation reduces the Asian summer monsoon and leads to easterly winds over the central SCS; as a result, diminished upwelling off the coast of Vietnam, with anticyclonic wind and ocean circulation, especially in the northern basin. The area of weakened WS gradually broadens to occupy the entire SCS with a lag of 8 months after the El Niño peak. Thus, anticyclonic wind and ocean circulation in the northern basin, diminished upwelling, and weakening WS over the entire basin are responsible for the low Chl *a* observed basin-wide due to a reduction in the nutrient supply from the deep layer, as indicated by a basin-wide increase in SST. Using lead-lag correlation analysis, we reveal the detailed spatiotemporal evolution of the biogeophysical environment throughout the SCS with respect to El Niño for the first time. The evolution of biogeophysical variables are responses to El Niño events of multiple types, but the precise difference between them is still under debate. Regardless of this debate, the central and eastern Pacific warmings likely influence the SCS in different ways, and it is thus worthwhile to separate and reanalyze this biogeophysical data only within periods of either central Pacific warming or eastern Pacific warming. Our suggestion for future work is to relate biogeophysical data sets during eastern Pacific warming period to Nino3 and those during central Pacific warming to the El Niño Modoki index over a decadal time scale, perhaps by assimilating satellite and marine ecosystem models. Thus, a more robust understanding of the specific spatiotemporal responses of the SCS biogeophysical environment to central Pacific warming or eastern Pacific warming can be gained.

Acknowledgments

This research was jointly supported by the Asia-Pacific Network for Global Change Research (APN, CAF2015-RR11-NMY-Siswanto), Guangdong Province of China (GDJ20154400004) and a Key Project of the National Natural Sciences Foundation of China (41430968). We thank the Ocean Biology Processing Group (OBPG) at the NASA Goddard Space Flight Center (Greenbelt, MD, USA), the NASA EOSDIS Physical Oceanography Distributed Active Archive Center (PO.DAAC) at the Jet Propulsion Laboratory (Pasadena, CA, USA), the National Center for Atmospheric Research (Boulder, CO, USA), Copernicus Marine Environment Service (CMEMS), and the Asia-Pacific Data Research Center (APDRC) for processing and distributing all data used in this study. The data used in this paper can be accessed from the following links: http://oceancolor.gsfc.nasa.gov for SeaWiFS Chl *a*, PAR, and MODIS SST; http://podaac.jpl.nasa.gov for AVHRR SST and CCMP wind fields; https://climatedataguide.ucar.edu for GLORS MLD; http://marine.copernicus.eu for SSH, http://apdrc.soest.hawaii.edu for TRMM RR, and http://www.cpc.ncep.noaa.gov/data/indices/sstoi.indices for Nino3.4.

References

Aita, M. N., Y. Yamanaka, and M. J. Kishi (2007), Interdecadal variation of the lower trophic ecosystem in the northern Pacific between 1948 and 2002, in a 3-D implementation of the NEMURO model, *Ecol. Modell.*, *202*, 81–94.

Alvera-Azcárate, A., A. Barth, and J. M. Beckers (2005), Reconstruction of incomplete oceanographic data sets using empirical orthogonal functions: Application to the Adriatic Sea surface temperature, *Ocean Modell.*, *9*(4), 325–346, doi:10.1016/j.ocemod.2004.08.001.

Ashok, K., S. K. Behera, S. A. Rao, H. Weng, and T. Yamagata (2007), El Nino Modoki and its possible teleconnection, *J. Geophys. Res.*, *112*, C11007, doi:10.1029/2006JC003798.

Behrenfeld, M. J., and P. G. Falkowski (1997), Photosynthetic rates derived from satellite-based chlorophyll concentration, *Limnol. Oceanogr.*, *42*(1), 1–20.

Behrenfeld, M. J., R. T. O'Malley, D. A. Siegel, C. R. McClain, J. L. Sarmiento, G. C. Feldman, A. J. Milligan, P. G. Falkowski, R. M. Letelier, and E. S. Boss (2006), Climate-driven trends in contemporary ocean productivity, *Nature*, *444*, 752–755, doi:10.1038/nature05317.

Chang, C.-W. J., H.-H. Hsu, C.-R. Wu, and W.-J. Sheu (2008), Interannual mode of sea level in the South China Sea and the roles of El Nino and El Nino Modoki, *Geophys. Res. Lett.*, *35*, L03601, doi:10.1029/2007GL032562.

Chen, Y.-L. L., H. Y. Chen, D. M. Karl, and M. Takahashi (2004), Nitrogen modulates phytoplankton growth in spring in the South China Sea, *Cont. Shelf Res.*, *24*, 527–541, doi:10.1016/j.csr.2003.12.006.

Deuser, W. G., F. E. Muller-Karger, R. H. Evans, O. B. Brown, W. E. Esaias, and G. C. Feldman (1990), Surface-ocean color and deep-ocean carbon flux: How close a connection? *Deep Sea Res., Part A*, *37*, 1331–1343.

Farr, T. G., et al. (2007), The Shuttle Radar Topography Mission, *Rev. Geophys.*, *45*, RG2004, doi:10.1029/2005RG000183.

Friedland, K. D., C. Stock, K. F. Drinkwater, J. S. Link, R. T. Leaf, B. V. Shank, J. M. Rose, C. H. Pilskaln, and M. J. Fogarty (2012), Pathways between primary production and fisheries yields of large marine ecosystem, *PLoS ONE*, *7*(1), e28945, doi:10.1371/journal.pone.0028945.

Gregg, W. W. (2008), Assimilation of SeaWiFS ocean chlorophyll data into a three-dimensional global ocean model, *J. Mar. Syst.*, *69*, 205–225.

Huot, Y., M. Babin, F. Bruyant, C. Grob, M. S. Twardowski, and H. Claustre (2007), Does chlorophyll *a* provide the best index of phytoplankton biomass for primary production studies?, *Biogeosci. Discuss.*, *4*, 707–745, doi:10.5194/bgd-4-707-2007.

Iverson, R. L. (1990), Control of marine fish production, *Limnol. Oceanogr.*, *35*, 1593–1604, doi:10.4319/lo.1990.35.7.1593.

Jing, Z., Y. Qi, and Y. Du (2011), Upwelling in the continental shelf of the northern South China Sea associated with 1997–1998 El Nino, *J. Geophys. Res.*, *116*, C02033, doi:10.1029/2010JC006598.

Karnauskas, K. B. (2013), Can we distinguished canonical El Nino from Modoki?, *Geophys. Res. Lett.*, *40*, 5246–5251, doi:10.1002/grl.51007.

Kim, H., P. J.-F. Yeh, T. Oki, and S. Kanae (2009), Role of rivers in the seasonal variations of terrestrial water storage over global basins, *Geophys. Res. Lett.*, *36*, L17402, doi:10.1029/2009GL039006.

Lan, J., Y. Wang, and Y. Bao (2012), Response of the South China Sea upper layer circulation to monsoon anomalies during 1997/1998 El Nino, *Aquat. Ecosyst. Health Manage.*, *15*(1), 6–13, doi:10.1080/14634988.2012.645750.

Large, W. G., and S. Pond (1981), Open ocean momentum flux measurements in moderate to strong winds, *J. Phys. Oceanogr.*, *11*, 324–336, doi:10.1175/1520-0485(1981)011<0324:OOMFMI>2.0.CO:2.

Lehner, B., and G. Grill (2013), Global river hydrography and network routing: Baseline data and new approaches to study the world's large river systems, *Hydrol. Proc.*, *27*(15), 2171–2186, doi:10.1002/hyp.9740.

Liao, X., J. Ma, and H. Zhan (2012), Effect of different types El Nino on primary productivity in the South China Sea, *Aquat. Ecosyst. Health*, *15*, 135–143, doi:10.1080/14634988.2012.687655.

Marathe, S., K. Ashok, P. Swapna, and T. P. Sabin (2015), Revisiting El Niño Modokis, *Clim. Dyn.*, *45*, 3527–3445.

Martinez, E., D. Antoine, F. D'Ortenzio, and B. Gentili (2009), Climate-driven basin-scale decadal oscillation of oceanic phytoplankton, *Science*, *326*, 1253–1256, doi:10.1126/science.1177012.

Nathans, L. L., F. L. Oswald, and K. Nimon (2012), Interpreting multiple linear regression: A guidebook of variable importance, *Pract. Assess. Res. Eval.*, *17*(9). [Available at http://pareonline.net/getvn.asp?v=17&n=9.]

Palacz, A. P., H. Xue, C. Armbrecht, C. Zhang, and F. Chai (2011), Seasonal and inter-annual changes in the surface chlorophyll of the South China Sea, *J. Geophys. Res.*, *116*, C09015, doi:10.1029/2011JC007064.

Rasanen, T. A., and M. Kummu (2013), Spatiotemporal influences of ENSO on precipitation and flood pulse in the Mekong River basin, *J. Hydrol.*, *476*, 154–168.

Siswanto, E., M. C. Honda, K. Matsumoto, Y. Sasai, T. Fujiki, K. Sasaoka, and T. Saino (2016a), Sixteen-year phytoplankton biomass trends in the northwestern Pacific Ocean observed by the SeaWiFS and MODIS ocean color sensors, *J. Oceanogr.*, *72*, 479–489, doi:10.1007/s10872-016-0357-1.

Siswanto, E., M. C. Honda, Y. Sasai, K. Sasaoka, and T. Saino (2016b), Meridional and seasonal footprints of the Pacific Decadal Oscillation on phytoplankton biomass in the northwestern Pacific Ocean, *J. Oceanogr.*, *72*, 465–477, doi:10.1007/s10872-016-0367-z.

Sun, C. (2017), Riverine influence on ocean color in the equatorial South China Sea, *Cont. Shelf Res.*, in press, doi:10.1016/j.csr.2016.10.008.

Takahashi, K., A. Montecinos, K. Goubanova, and B. Dewitte (2011), ENSO regimes: Reinterpreting the canonical and Modoki El Nino, *Geophys. Res. Lett.*, *38*, L10704, doi:10.1029/2011GL047364.

Tan, S. C., and G. Y. Shi (2009), Spatiotemporal variability of satellite-derived primary production in the South China Sea, 1998–2006, *J. Geophys. Res.*, *114*, G03015, doi:10.1029/2008JG000854.

Tang, D, H. Kawamura, T. V. Dien, and M. Lee (2004), Offshore phytoplankton biomass increase and its oceanographic causes in the South China Sea, *Mar. Ecol. Prog. Ser.*, *268*, 31–41.

Wang, C., W. Wang, D. Wang, and Q. Wang (2006), Interannual variability of the South China Sea associated with El Nino, *J. Geophys. Res.*, *111*, C03023, doi:10.1029/2005JC003333.

Wang, J., D. Tang, and Y. Sui (2010), Winter phytoplankton bloom induced by subsurface upwelling and mixed layer entrainment southwest of Luzon Strait, *J. Mar. Syst.*, *83*, 141–149.

Wu, C.-R., and C.-W. J. Chang (2005), Interannual variability of the South China Sea in a data assimilation model, *Geophys. Res. Lett.*, *32*, L17661, doi:10.1029/2005GL023798.

Wu, J., S.-W. Chung, L.-S. Wen, K.-K. Liu, Y.-L. L. Chen, H.-Y. Chen, and D. M. Karl (2003), Dissolved inorganic phosphorus, dissolved iron, and *Trichodesmium* in the oligotrophic South China Sea, *Global Biogeochem. Cycles*, *17*(1), 1008, doi:10.1029/2002GB001924.

Xie, S. P., Q. Xie, D. Wang, and W. T. Liu (2003), Summer upwelling in the South China Sea and its role in the regional climate variations, *J. Geophys. Res.*, *108*(C8), 3261, doi:10.1029/2003JC001867.

Yamazaki, D., S. Kanae, H. Kim, and T. Oki (2011), A physical based description of floodplain inundation dynamics in a global river model, *Water Resour. Res.*, *47*, W04501, doi:10.1029/2010WR009726.

Yamazaki, D., G. A. M. de Almeida, and P. D. Bates (2013), Improving computational efficiency in global river models by implementing the local inertial flow equation and a vector-based river network map, *Water Resour. Res.*, *49*, 7221–7235, doi:10.1002/wrcr.20552.

Yan, Y., Z. Ling, and C. Chen (2015), Winter coastal upwelling off northwest Borneo in the South China Sea, *Acta Oceanol. Sin.*, *34*, 3–10.

Zhao, H., and D. Tang (2007), Effect of 1998 El Nino on the distribution of phytoplankton in the South China Sea, *J. Geophys. Res.*, *112*, C02017, doi:10.1029/2006JC003536.